JCI The Journal of Clinical Investigation

Impact of TREM2^{R47H} variant on tau pathology–induced gliosis and neurodegeneration

Maud Gratuze, … , Jason D. Ulrich, David M. Holtzman

J Clin Invest. 2020;130(9):4954-4968. https://doi.org/10.1172/JCI138179.

Research Article | Inflammation | Neuroscience

Graphical abstract

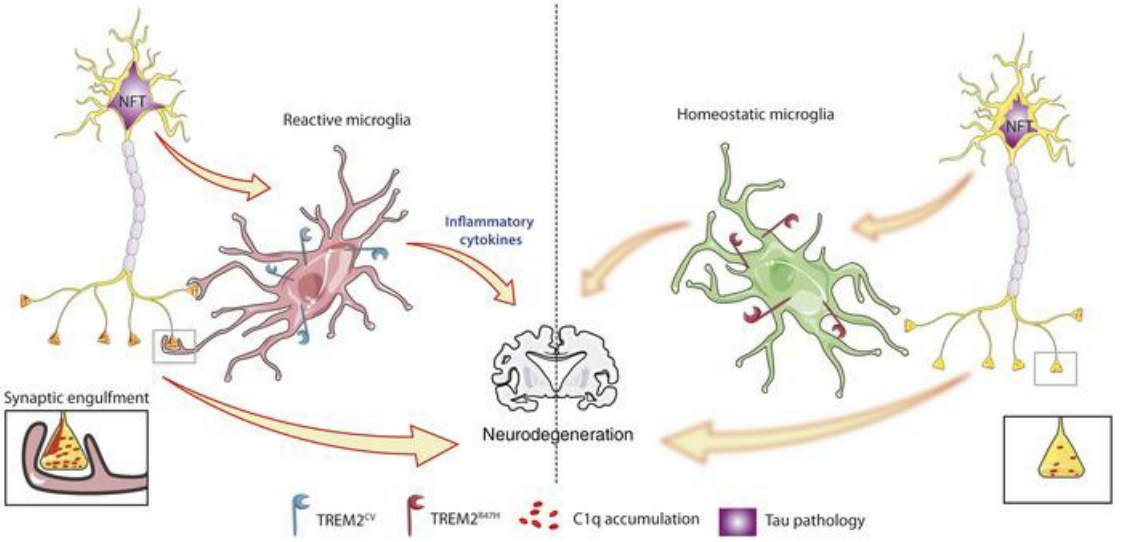

Impact of TREM2^{R47H} variant on tau pathology–induced gliosis and neurodegeneration

Maud Gratuze,[1,2,3] Cheryl E.G. Leyns,[1,2,3] Andrew D. Sauerbeck,[1] Marie-Kim St-Pierre,[4,5] Monica Xiong,[1,2,3] Nayeon Kim,[1,2,3] Javier Remolina Serrano,[1,2,3] Marie-Ève Tremblay,[4,5] Terrance T. Kummer,[1] Marco Colonna,[2,3,6] Jason D. Ulrich,[1,2,3] and David M. Holtzman[1,2,3]

[1]Department of Neurology, [2]Hope Center for Neurological Disorders, and [3]Knight Alzheimer's Disease Research Center, Washington University School of Medicine, St. Louis, Missouri, USA. [4]Axe Neurosciences, Centre de Recherche, Centre Hospitalier Universitaire (CHU) de Québec-Université Laval, Québec City, Québec, Canada. [5]Division of Medical Sciences, University of Victoria, Victoria, British Columbia, Canada. [6]Department of Pathology and Immunology, Washington University School of Medicine, St. Louis, Missouri, USA.

Alzheimer's disease (AD) is characterized by plaques containing amyloid-β (Aβ) and neurofibrillary tangles composed of aggregated, hyperphosphorylated tau. Beyond tau and Aβ, evidence suggests that microglia play an important role in AD pathogenesis. Rare variants in the microglia-expressed triggering receptor expressed on myeloid cells 2 (*TREM2*) gene increase AD risk 2- to 4-fold. It is likely that these TREM2 variants increase AD risk by decreasing the response of microglia to Aβ and its local toxicity. However, neocortical Aβ pathology occurs many years before neocortical tau pathology in AD. Thus, it will be important to understand the role of TREM2 in the context of tauopathy. We investigated the impact of the AD-associated TREM2 variant (R47H) on tau-mediated neuropathology in the PS19 mouse model of tauopathy. We assessed PS19 mice expressing human TREM2^{CV} (common variant) or human TREM2^{R47H}. PS19-TREM2^{R47H} mice had significantly attenuated brain atrophy and synapse loss versus PS19-TREM2^{CV} mice. Gene expression analyses and CD68 immunostaining revealed attenuated microglial reactivity in PS19-TREM2^{R47H} versus PS19-TREM2^{CV} mice. There was also a decrease in phagocytosis of postsynaptic elements by microglia expressing TREM2^{R47H} in the PS19 mice and in human AD brains. These findings suggest that impaired TREM2 signaling reduces microglia-mediated neurodegeneration in the setting of tauopathy.

Introduction

Alzheimer's disease (AD) is the leading cause of dementia worldwide and is the sixth leading cause of death in the United States (1). The histopathological hallmarks of AD are extracellular amyloid plaques composed predominantly of the amyloid-β (Aβ) peptide and neurofibrillary tangles (NFTs) within neurons consisting of abnormally aggregated, hyperphosphorylated tau protein (for reviews, refs. 2–4). Beyond tau and Aβ pathologies, neuroinflammatory changes are present in AD and in primary tauopathies (5), including alterations in the morphology, reactivity, distribution, and gene expression of microglia. The gene expression changes that occur in microglia in the presence of amyloid, tau, and other pathologies have been termed by some as disease-associated microglia (DAM) (6) or the microglial neurodegenerative (MGnD) phenotype (7). In the DAM and MGnD phenotypes, there is a downregulation of so-called homeostatic microglial genes such as *P2ry12*, *Tmem119*, and *Cx3cr1*, while there is an increase in the expression of several other genes such as *Apoe*, *Tyrobp*, and *Trem2* (6, 7). However, the exact contributions of innate immune activation to different types of pathologies and neurodegeneration are still not clear.

In the last decade, several novel genetic factors linked with increased risk of AD have been identified thanks to new whole-genome sequencing and genome-wide association studies (GWAS). Interestingly, many of these genetic risk factors encode proteins involved in microglial function and inflammation including triggering receptor expressed on myeloid cells 2 (TREM2), CD33, CR1, ABCA7, SPI1, and SHIP1 (8). Particular interest has been given to the microglia-expressed TREM2, since rare variants in the *TREM2* gene increase AD risk 2- to 4-fold (9, 10). TREM2 is a receptor that belongs to the immunoglobulin superfamily and is expressed on myeloid cells such as microglia in the brain (11, 12). TREM2 signaling is associated with a number of downstream cellular processes including proliferation and survival, suppression of Toll-like receptor–induced inflammatory cytokine production, and facilitation of metabolic ATP production (13). Several TREM2 variants have been shown to impair, but not block, functional TREM2 signaling, resulting in the partial loss of function of the receptor. The most common AD-associated TREM2 variant is rs75932628, a single-nucleotide polymorphism encoding an arginine-to-histidine missense substitution at amino acid 47 (R47H)

Conflict of interest: DMH and JDU are listed as inventors on a provisional patent from Washington University on TREM2 antibodies. DMH and CEGL are listed as inventors on a patent licensed by Washington University to C2N Diagnostics on the therapeutic use of anti-tau antibodies. CEGL is currently an employee at Merck. MC receives research funding from Alector, Amgen, and Ono. DMH cofounded and is on the scientific advisory board of C2N Diagnostics. C2N Diagnostics has licensed certain anti-tau antibodies to AbbVie for therapeutic development. DMH is on the scientific advisory board of Denali and consults for Genentech and Idorsia.

Submitted: March 16, 2020; **Accepted:** June 10, 2020; **Published:** August 17, 2020.
Reference information: *J Clin Invest*. 2020;130(9):4954–4968.
https://doi.org/10.1172/JCI138179.

(9, 10). The TREM2^{R47H} variant results in decreased TREM2 signaling upon ligand-induced stimulation (14, 15).

In order to better understand the role of TREM2 and AD-associated *TREM2* variants in AD pathogenesis, several studies have used models of AD pathology. In vivo studies in mouse models of amyloid deposition indicate a critical function for TREM2 in the clustering of microglia around plaques, plaque compaction, microglial proliferation, and phagocytosis, and in decreasing Aβ-induced neuritic dystrophy and tau seeding/spreading. TREM2 knockout or expression of the TREM2^{R47H} variant have been shown to affect these phenotypes in the opposite direction (14–18). These studies suggest that TREM2 signaling is protective in decreasing Aβ-mediated local injury and in exacerbating the Aβ-induced spreading of tau pathology. However, in AD and in primary tauopathies, the accumulation of aggregated, hyperphosphorylated tau, and not Aβ, strongly correlates with local brain atrophy and neuronal death. In AD, the accumulation of pathological forms of tau in the neocortex associated with atrophy and cell death does not begin to occur until about 15–25 years after the onset of Aβ deposition (19). The role of TREM2 and *TREM2* variants linked to AD in the setting of tauopathy has been much less studied. However, numerous clues in the literature suggest a link between tau pathology and TREM2 in AD. In the cerebrospinal fluid (CSF) of AD patients, soluble TREM2 has been shown to correlate with total and phosphorylated tau (p-tau, Thr181) levels (20, 21). Moreover, AD patients harboring the R47H variant of TREM2 display higher levels of both total tau and p-tau (Thr181) in CSF compared with noncarriers (22, 23). Importantly, levels of p-tau in the CSF correlate with tau pathology burden in the brain and with neuronal loss and cognitive decline in AD patients (24). Previously, we reported a decrease in brain atrophy as well as attenuated microgliosis in the brains of PS19 mice lacking TREM2 without a significant change in tau pathology (25). In another study, Sayed et al. also found that TREM2 knockout protected against tau-mediated microglial reactivity and atrophy (25), but that TREM2 haploinsufficiency was associated with elevated expression of proinflammatory markers, exacerbated atrophy, and increased tau pathology in PS19 mice (26). Finally, Bemiller et al. crossed TREM2 knockout mice with mice expressing human tau (hTau mice), a less aggressive mouse model of tauopathy, and identified a decrease in microgliosis in TREM2-deficient hTau mice (27), as observed in TREM2-deficient PS19 mice, but reported that complete deletion of TREM2 in hTau mice exacerbated tau pathology–related markers. These studies in primary tauopathy mouse models suggest that TREM2 may play a dual role depending on the disease stages; during early stages of tau pathology development in the absence of neurodegeneration (e.g., hTau mice), decreased TREM2 function might promote tau pathology, whereas the complete loss of TREM2 function in advanced stages (PS19 mice) of the disease seems to protect from neurodegeneration. However, no study to our knowledge has evaluated the impact of AD-associated TREM2 variants, such as TREM2^{R47H}, in the setting of a model of pure tauopathy, nor in a model that develops robust neurodegeneration as is seen in tau-related neurodegenerative diseases.

Given the emerging role for microglia in tau-mediated neuropathology, it is important to understand the role of AD-associated *TREM2* variants that decrease, but do not eliminate, TREM2 signaling in the context of tauopathy and its associated neurodegeneration. Therefore, we investigated the impact of the most prominent AD-associated *TREM2* variant (R47H) on tau pathology and tau-mediated brain damage in the PS19 mouse model of tauopathy. PS19 mice were crossed with mice expressing human TREM2 common variant, TREM2^{CV} (PS19-T2^{CV} mice), or human TREM2^{R47H} lacking the endogenous murine *Trem2* gene (PS19-T2^{R47H} mice). We hypothesized that TREM2^{R47H} would result in a decreased microglial inflammatory response and would protect against tau-dependent neurodegeneration. We observed that PS19-T2^{R47H} mice have reduced p-tau staining compared with PS19-T2^{CV} mice. Moreover, PS19-T2^{R47H} mice have significantly attenuated brain atrophy and synapse loss compared with PS19-T2^{CV} mice. Gene expression analyses and CD68 immunostaining revealed attenuated microglial reactivity in PS19-T2^{R47H} versus PS19-T2^{CV} mice. Importantly, a decrease in phagocytosis of postsynaptic elements by microglia expressing TREM2^{R47H} was detected in PS19 mice and in postmortem human AD brains. Collectively, these findings suggest that reduced TREM2 signaling reduces microglial conversion to a more proinflammatory, phagocytic state and is protective against neurodegeneration in the setting of advanced tauopathy.

Results

Effects of TREM2^{R47H} on p-tau pathology. To determine whether the presence of the R47H variant of TREM2 affects tau pathology and tau-related inflammation and neurodegeneration, we used the PS19 tauopathy mouse model that overexpresses 1N4R hTau containing the P301S mutation that causes a familial form of frontal temporal dementia. By 9 months of age, this model develops strong tau hyperphosphorylation and aggregation, neurofibrillary tangle deposition, and gliosis, as well as neuronal loss, brain atrophy, and loss of synaptic proteins in specific brain regions including the hippocampus, entorhinal cortex, piriform cortex, and amygdala (28, 29). We crossed PS19 mice on a mouse TREM2-KO background with bacterial artificial chromosome (BAC) transgenic mouse lines expressing either human TREM2^{CV} or the AD-associated human variant TREM2^{R47H} on a mouse TREM2-KO background (15). Importantly, TREM2^{CV} and TREM2^{R47H} mice express a similar level of TREM2 protein in the brain and expression of TREM2^{CV}, but not TREM2^{R47H}, rescues TREM2-dependent phenotypes such as plaque-associated microgliosis (15).

At 3 months of age, before the overt onset of tau pathology, we observed reduced staining with an antibody (AT8) specific for p-tau phosphorylated on serine 202 and threonine 205 (p.Ser202/p.Thr205), in the hippocampus (Supplemental Figure 1, B and D; supplemental material available online with this article; https://doi.org/10.1172/JCI138179DS1) and piriform cortex (Supplemental Figure 1, A and C) of PS19-T2^{R47H} mice compared with PS19-T2^{CV} mice, although the change was only statistically significant in the hippocampus. Staining with antibodies AT180 (p.Thr231) and PG5 (p.Ser409) did not reveal any significant differences in p-tau between PS19-T2^{R47H} mice and PS19-T2^{CV} mice in the piriform cortex (Supplemental Figure 1, E, G, I, and K) or hippocampus (Supplemental Figure 1, F, H, J, and L). To further examine tau and p-tau levels in these mice, we performed a biochemical extraction of hippocampal brain tissue and measured the concentration of

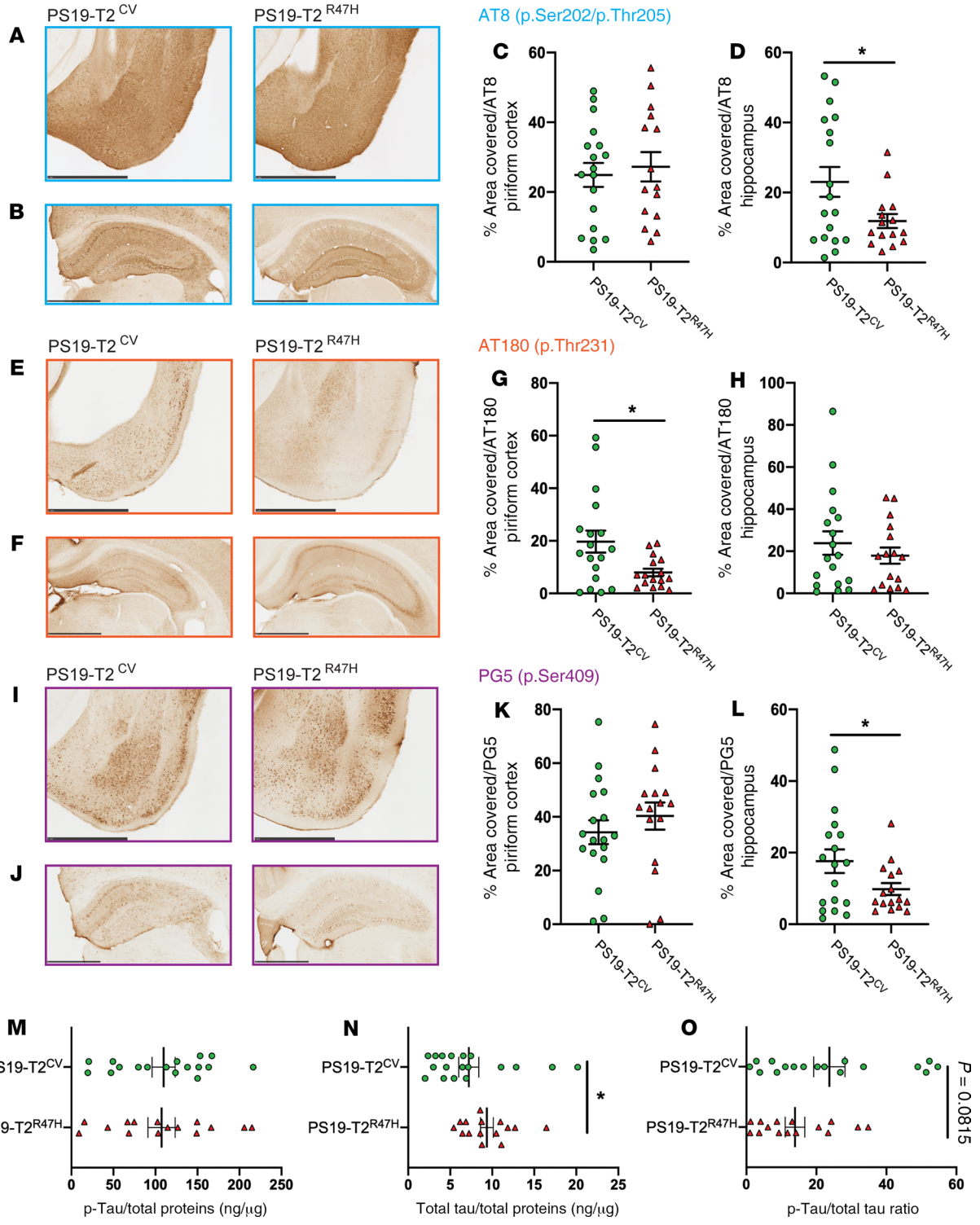

Figure 1. R47H variant of TREM2 attenuates tau pathology in 9-month-old PS19 mice. Representative images of p-tau staining (AT8, AT180, and PG5) in the piriform cortex (**A**, **E**, and **I**) and hippocampus (**B**, **F**, and **J**) from 9-month-old PS19-T2^{CV} and PS19-T2^{R47H} mice. Scale bars: 1 mm. Quantification of the percentage area covered by p-tau staining (antibodies AT8, AT180, and PG5) in the piriform cortex (**C**, **G**, and **K**) and hippocampus (**D**, **H**, and **L**). Data are presented as the mean ± SEM. Significance was determined using an unpaired, 2-tailed Mann-Whitney test due to the nonparametric data set, except for PG5 staining in the hippocampus where an unpaired, 2-tailed *t* test with Welch's correction was used due to significantly different variances. *$P < 0.05$ (PS19-T2^{CV}, $n = 18$ and PS19-T2^{R47H}, $n = 15/16$). (**M**–**O**) ELISA results showing concentrations of p-tau (p.Ser202/p.Thr205 and p.Thr181) and total tau and p-tau/total tau ratio in the hippocampus were quantified using a human tau–specific (hTau-specific) sandwich ELISA to measure p-tau (**M**), total tau (**N**), and the p-tau/total tau ratio (**O**). The levels of p-tau and total tau (**M** and **N**) were normalized to total protein concentration. Data are presented as mean ± SEM. Significance was determined by an unpaired, 2-tailed Student's *t* test except for total tau where an unpaired, 2-tailed Mann-Whitney test was used due to the nonparametric data set. *$P < 0.05$ (PS19-T2^{CV}, $n = 17$ and PS19-T2^{R47H}, $n = 15$).

p-tau and total tau using a p-tau–specific (p.Ser202/p.Thr205 and p.Thr181) and hTau-specific ELISA. We observed no significant differences in p-tau (Supplemental Figure 1M) and tau levels (Supplemental Figure 1N) or in the p-tau/tau ratio (Supplemental Figure 1O) between PS19-T2^{R47H} mice and PS19-T2^{CV} mice. At 9 months of age, when substantial tau pathology had developed, we again observed a significant decrease in hippocampal p-tau staining on serine 202/threonine 205 (Figure 1, B and D) as well as on serine 409 (Figure 1, J and L) between PS19-T2^{R47H} and PS19-T2^{CV} mice. There was no significant difference observed on these p-tau epitopes in the piriform cortex (Figure 1, A, C, I, and K). Interestingly, staining p-tau on threonine 231 revealed less p-tau in the piriform cortex of PS19-T2^{R47H} mice compared with PS19-T2^{CV} mice (Figure 1, F and H), but no difference in the hippocampus (Figure 1, E and G). Biochemical analysis of p-tau in hippocampal brain tissue samples by ELISA revealed no significant differences in p-tau level (Figure 1M) but increased total tau levels in PS19-T2^{R47H} mice compared with PS19-T2^{CV} mice (Figure 1N), resulting in a slight but not statistically significant ($P = 0.0815$) decrease in the p-tau/tau ratio (Figure 1O) in PS19-T2^{R47H} mice compared with PS19-T2^{CV} mice. These findings demonstrate that the R47H variant of TREM2 significantly attenuates increases in p-tau on some tau sites mostly in the later stages of tau pathology in PS19 mice. Interestingly, we (25) and others (27) did not observe lower p-tau pathology in PS19 mice with TREM2 deleted compared with PS19 mice. New studies will be needed to better understand this difference, but we can hypothesize that the human TREM2^{CV} assessed in the present study has a slightly different impact on tau pathology than mouse TREM2 used in the previous studies.

Effects of TREM2^{R47H} on brain atrophy. Because pathological tau is directly linked to neurodegeneration, we next evaluated the brain volume of these mice. As expected, no change in brain volume was detected between PS19-T2^{R47H} and PS19-T2^{CV} mice at 3 months of age, which is before when neurodegeneration has been observed in this model (Supplemental Figure 2, A–E). At 9 months of age when tau pathology is much more substantial and neurodegeneration is usually marked in specific brain regions in this model, the presence of TREM2^{R47H} strongly attenuated brain atrophy in PS19 mice compared with mice expressing TREM2^{CV} (Figure 2, A and E), similar to PS19 mice lacking TREM2 (25). More specifically, atrophy was significantly decreased by approximately 24% in the hippocampus (Figure 2B) and by approximately 34% in the piriform and entorhinal cortices (Figure 2D). When atrophy occurs in hippocampal and cortical regions, there is concomitant enlargement of the lateral ventricles. TREM2^{R47H} was also associated with extensively reduced ventricular dilatation (~67%) in 9-month-old PS19 mice (Figure 2C). Then, we estimated the neuronal loss by measuring the thickness of the granule cell layer in the dentate gyrus and the pyramidal cell layer in the piriform cortex in 9-month-old mice. In accordance with changes observed in brain volume, both the granule cell layer in the dentate gyrus (Figure 2, G and I) and pyramidal cell layer in the piriform cortex (Figure 2, F and H) were visibly and significantly thicker in PS19-T2^{R47H} compared with PS19-T2^{CV} mice. This strikingly reduced neurodegeneration suggests an important role for TREM2 in regulating tau-mediated brain atrophy, with the R47H variant of TREM2 being neuroprotective in the setting of tauopathy.

Effects of TREM2^{R47H} on microglial and astrocytic phenotypes. Microglia are critical mediators of tau-dependent neurodegeneration (28, 30). Given that the TREM2^{R47H} variant affects microglial function, and that PS19-T2^{R47H} mice exhibited reduced neurodegeneration, we hypothesized that we would also observe a state of reduced microglial reactivity as reflected by staining with certain microglial markers. We assessed brain sections with the myeloid immune cell marker ionized calcium–binding adaptor molecule 1 (Iba1) to assess the overall microglial population. At 3 months of age, before the onset of overt tau pathology, there was no change in the surface area covered by microglia in the piriform cortex (Supplemental Figure 3, A and C) or the hippocampus (Supplemental Figure 3, B and D) between PS19-T2^{R47H} and PS19-T2^{CV} mice. When we assessed microglial coverage in 9-month-old mice, we observed a marked decrease in Iba1 staining in the piriform cortex (Figure 3, B and D) and the hippocampus (Figure 3, C and E) of PS19-T2^{R47H} in comparison with PS19-T2^{CV} mice. Consistent with these results, Iba1 gene expression was reduced by approximately 32% in the cortex of PS19-T2^{R47H} versus PS19-T2^{CV} mice (Figure 3A). Importantly, reduced microgliosis induced by TREM2^{R47H} in PS19 mice was qualitatively similar to previous observations when TREM2 was deleted in the same mouse model (25).

We next assessed microglial phenotypic and functional changes in the mice (Figure 4). CD68 (cluster of differentiation 68) labeling, a marker of phagolysosomal activity, was drastically reduced in the piriform cortex (Figure 4C) and the hippocampus (Figure 4D) of 9-month-old PS19-T2^{R47H} compared with PS19-T2^{CV} mice. Strikingly, there was a decrease in CD68 staining of approximately 78% per Iba1^{+} cell volume detected in PS19-T2^{R47H} versus PS19-T2^{CV} brains (Figure 4, E and F), confirming a reduced activation state of PS19-T2^{R47H} microglia. We also assessed the microglial gene expression profile in the cortex of 9-month-old PS19-T2^{R47H} and PS19-T2^{CV} mice (Figure 4G). Consistent with lower CD68 staining in PS19-T2^{R47H} mice, all the DAM genes tested were downregulated in PS19-T2^{R47H} compared with PS19-T2^{CV} mice such as *Axl*, *Cst7*, and *Cd9*. Interestingly, an increase in the expression of the homeostatic gene *P2ry12* was observed in PS19-T2^{R47H} mice, suggesting a more homeostatic status of microglia compared with PS19-T2^{CV} mice. On the other hand, *Cx3cr1* gene expression was decreased in PS19 mice expressing TREM2^{R47H}, which may be due to a lower number of microglia in these mice. Evaluation of several inflammatory cytokine genes revealed a significant decrease in proinflammatory mediators such as IL-1α, IL-1β, TNF-α, and TGF-β. IL-6 gene expression was not altered by the AD-associated TREM2 variant in PS19 mice, as previously reported in PS19 knockout for TREM2 (25).

Another brain cell type, astrocytes, also plays an essential role in neuroinflammation. It has been previously shown that reactive microglia can induce astrogliosis through the production of cytokines as IL-1α and TNF-α that can promote neuronal death (32, 33). As previously observed in PS19 mice lacking TREM2 (25), we found that glial fibrillary acidic protein (GFAP) gene expression, a marker of reactive astrocytes, was decreased in 9-month-old PS19-T2^{R47H} compared with PS19-T2^{CV} mice (Supplemental Figure 4A). In addition, the GFAP signal was drastically reduced in the piriform cortex (Supplemental Figure 4, B and D) of PS19-T2^{R47H} compared with PS19-T2^{CV} mice, but

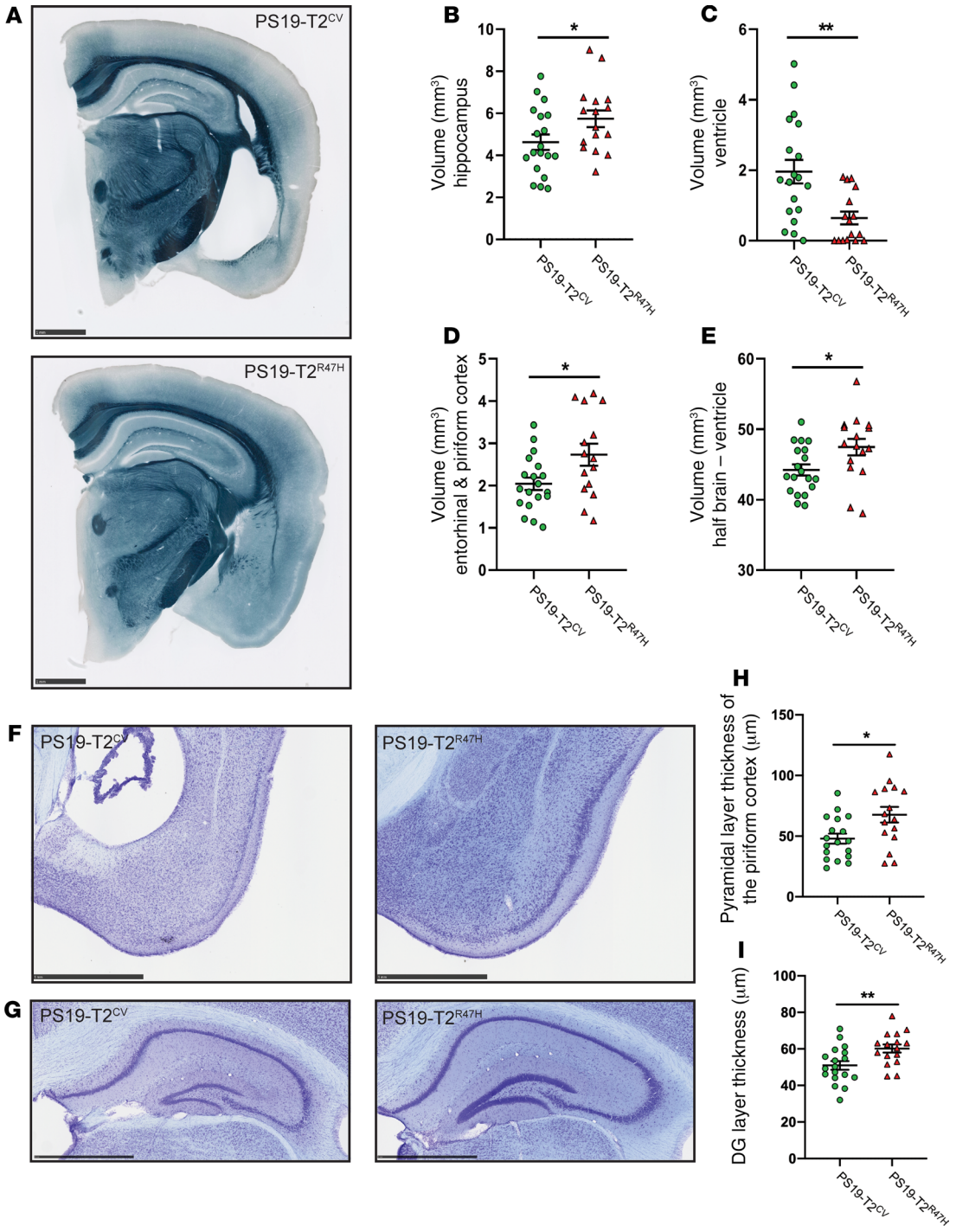

Figure 2. R47H variant of TREM2 decreases neurodegeneration in 9-month-old PS19 mice. (**A**) Representative images of PS19-T2^{CV} and PS19-T2^{R47H} brain sections stained with Sudan black at 9 months of age. Scale bars: 1 mm. (**B**–**E**) Quantification of the average volume of the hippocampus (**B**), ventricles (**C**), entorhinal and piriform cortices (**D**), and half brain minus ventricle (**E**). (**F**–**I**) Thickness of the pyramidal layer of the piriform cortex (**F** and **H**) and the granule cell layer of the dentate gyrus (DG) (**G** and **I**) in 9-month-old mice with cresyl violet staining. Data are presented as mean ± SEM. Significance was determined by an unpaired, 2-tailed Student's *t* test. $^*P < 0.05$, $^{**}P < 0.01$ (9-month-old: PS19-T2^{CV}, $n = 18/19$ and PS19-T2^{R47H}, $n = 16$).

not in the hippocampus (Supplemental Figure 4, E and C). Taken together, these data suggest that the R47H variant of TREM2 strongly reduced microglial activation and the concomitant astrogliosis in the setting of tauopathy.

Effects of TREM2^{R47H} on synapses. A recent study by Dejanovic et al. reported a striking accumulation of complement C1q in synapses of PS19 mice and AD patients (34). Synaptic C1q accumulation correlated with augmented microglial engulfment of synapses in vivo and decline of synapse density in vitro. Because we previously showed that *C1q* gene expression can be modulated by the absence of TREM2 in PS19 mice, we assessed how TREM2^{R47H} affected protein and gene expression

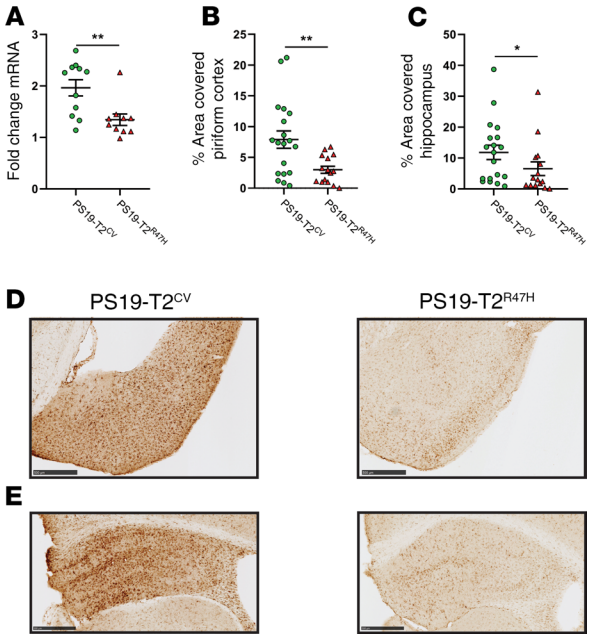

Figure 3. R47H variant of TREM2 decreases microgliosis in 9-month-old PS19 mice. (**A**) Expression of microglial marker Iba1 in the cortex of 9-month-old PS19-T2^{CV} and PS19-T2^{R47H} mice (PS19-T2^{CV}, n = 11 and PS19-T2^{R47H}, n = 10). (**B** and **C**) Quantification of the percentage area covered by Iba1 staining in the piriform cortex (**B**) and hippocampus (**C**) (PS19-T2^{CV}, n = 19 and PS19-T2^{R47H}, n = 18). (**D** and **E**) Representative images of Iba1 staining in the piriform cortex (**D**) and hippocampus (**E**) from PS19-T2^{CV} and PS19-T2^{R47H} mice. Scale bars: 0.5 mm. Data are presented as mean ± SEM. Significance was determined using an unpaired, 2-tailed Mann-Whitney test due to the nonparametric data set. *P < 0.05, **P < 0.01.

levels of *C1q*, as well as C1q$^+$ synapses in PS19 mice. First, we found that *C1qa* gene expression was reduced by approximately 60% in the cortex of 9-month-old PS19-T2^{R47H} compared with the PS19-T2^{CV} mice (Figure 5C). Consistent with these findings, C1q staining and confocal analysis revealed reduced C1q staining in PS19-T2^{R47H} mice (Figure 5B). To evaluate C1q accumulation at putative synapses, we then assessed the number of puncta labeled with pre- and postsynaptic markers that were positive for C1q. PSD-95$^+$ puncta and synapsin$^+$ puncta positive for C1q were significantly decreased in PS19-T2^{R47H} versus PS19-T2^{CV} mice (Figure 5, A, D, and E).

We next assessed whether the decrease in C1q-opsonized synaptic-marker puncta and attenuated brain atrophy would correspond to improved synaptic integrity in PS19-T2^{R47H} mice. We therefore quantified presynaptic (synapsin) and postsynaptic (PSD-95) marker puncta in PS19-T2^{R47H} and PS19-T2^{CV} mice in the polymorphic layer of the piriform cortex (Figure 6A). This revealed significantly more pre- and postsynaptic puncta in PS19-T2^{R47H} compared with PS19-T2^{CV} mice (Figure 6, B and C). As many such puncta are nonsynaptic (35, 36), we turned to a more specific method of quantifying intact synaptic loci. Using SEQUIN analysis (synaptic evaluation and quantification by imaging of nanostructure) (36), a super-resolution imaging and image analysis platform for quantifying synaptic loci, we detected significantly more intact synaptic loci in PS19-T2^{R47H} versus PS19-T2^{CV} mice (Figure 6D). To better understand ultrastructural changes at synapses under these conditions, electron microscopy was undertaken in a small parallel cohort in the polymorphic layer of the piriform cortex. Synapses from PS19-T2^{CV} mice exhibited several dystrophic features, including swollen presynaptic elements, accumulation of enlarged autophagosomes, and a reduced number of synaptic vesicles (Figure 6E). Moreover, mitochondria often appeared swollen, a feature also seen with hypoxia, and abundant dark dendritic spines, indicative of postsynaptic cellular stress, were visible (Figure 6E). In contrast, electron microscopic images from PS19-T2^{R47H} mice revealed improved synaptic integrity with fewer autophagosomes, preserved mitochondrial ultrastructure, and less frequent dark dendrites/spines and axon terminals (Figure 6F). Importantly, these results demonstrate that reduced brain atrophy in PS19-T2^{R47H} mice is associated with decreased synapses with dystrophic features and better preservation of pre- and postsynaptic elements.

Effects of TREM2^{R47H} on microglial phagocytosis of synaptic elements. Regarding the role of TREM2 in microglial phagocytosis (37, 38) and the fact that we observed strong reduction of CD68$^+$ phagolysosomes in microglia of PS19-T2^{R47H} versus PS19-T2^{CV} mice, we then hypothesized that impairment of microglial phagocytosis in 9-month-old PS19-T2^{R47H} mice is responsible for the decreased synapse loss. A previous study by Filipello et al. (39) demonstrating that microglial TREM2 is required for synapse elimination during the early stages of brain development strongly support this hypothesis. Costaining and confocal analysis for the microglial phagolysosomal marker CD68 and the postsynaptic marker PSD-95 revealed significantly fewer PSD-95 puncta in CD68$^+$ vesicles per microglia in the polymorphic layer of the piriform cortex of 9-month-old PS19-T2^{R47H} compared with PS19-T2^{CV} mice (Figure 7, A and B). Consistent with the higher content of synapses in 9-month-old PS19-T2^{R47H} mice, these data show an important role for TREM2 in synapse loss in PS19 mice that is decreased by TREM2^{R47H} in a pure tauopathy model.

Given these results, to assess the relevance of these findings in the setting of tauopathy in human AD, we assessed whether the brains of individuals who were TREM2-variant carriers who had AD exhibited similar reductions of postsynaptic puncta engulfed in CD68$^+$ phagolysosomes compared with AD cases expressing TREM2^{CV}. We stained prefrontal cortex tissue from late-onset AD TREM2^{R47H} and TREM2^{R62H} individuals and their case-matched controls for Iba1, CD68, and PSD-95. R62H is another TREM2 variant associated with an increased risk for AD (40, 41). Consistent with our mouse data, we detected significantly fewer PSD-95 puncta engulfed in CD68$^+$ vesicles per microglia in AD TREM2^{R47H} and TREM2^{R62H} brains compared with AD brains with TREM2^{CV} (Figure 7, C and D). The detection of reduced synaptic phagocytosis by microglia expressing R47H or R62H variants of TREM2 in AD cases confirms the defective synapse elimination by microglia with TREM2 loss of function. Taken together, these data suggest that microglia expressing TREM2^{R47H} phagocytose fewer synapses due to lower C1q accumulation in synapses, resulting in neuroprotection in the setting of tauopathy.

Discussion

TREM2^{R47H} has been associated with higher risk of developing AD. Data from animal models and humans suggest that the

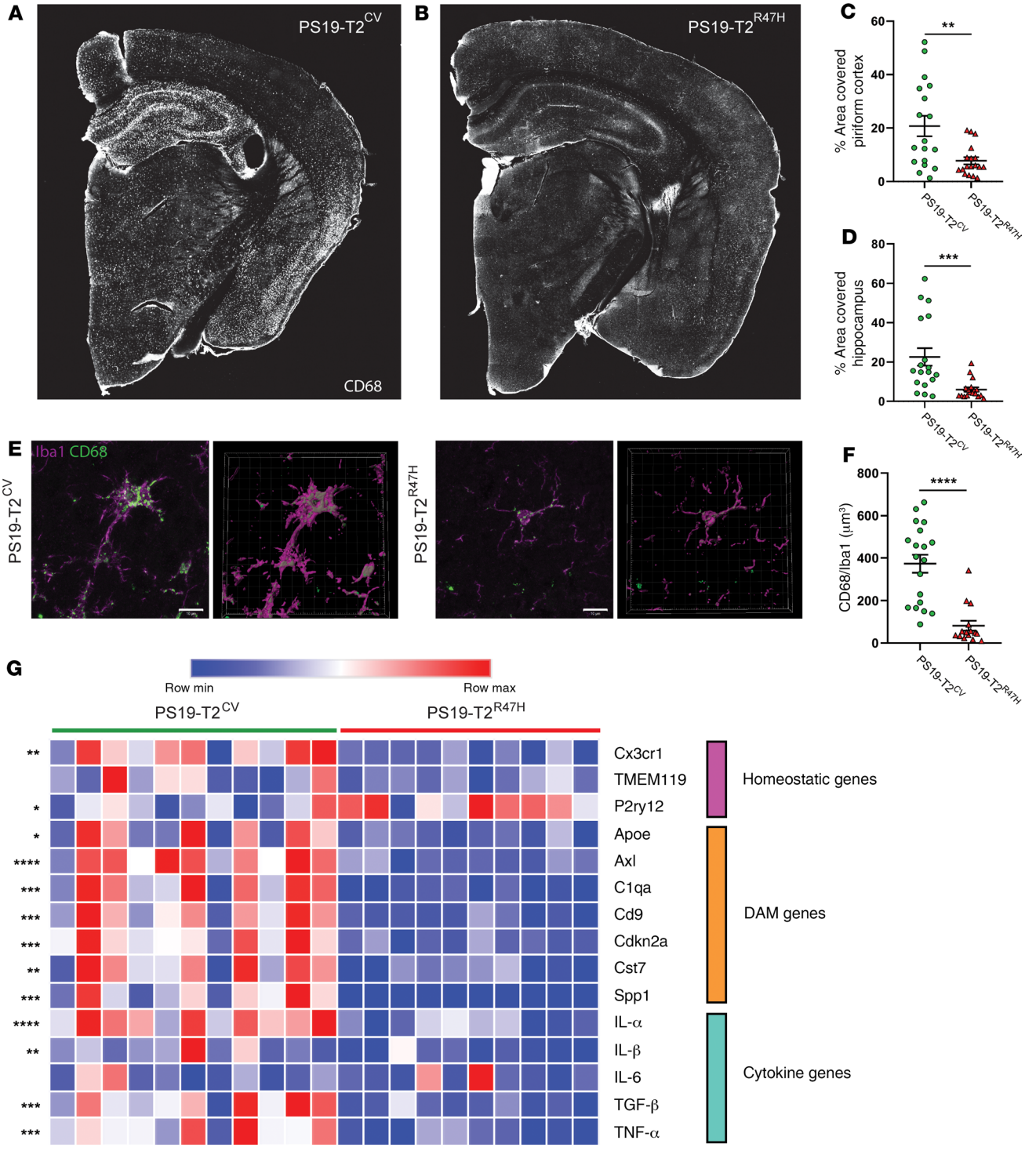

Figure 4. Reduced microglial activation and inflammatory gene expression in 9-month-old PS19-T2^{R47H} versus PS19-T2^{CV} mice. (**A** and **B**) Representative images of CD68 staining from 9-month-old PS19-T2^{CV} (**A**) and PS19-T2^{R47H} (**B**) brains. (**C** and **D**) Quantification of the percentage area covered by CD68 staining in the piriform cortex (**C**) and hippocampus (**D**) (PS19-T2^{CV}, $n = 18$ and PS19-T2^{R47H}, $n = 18$). (**E**) Confocal images and 3D reconstruction of CD68$^+$ structures within Iba1$^+$ microglia in PS19-T2^{CV} and PS19-T2^{R47H}. Scale bars: 10 μm. (**F**) Quantification of CD68$^+$ structures per Iba1 volume (PS19-T2^{CV}, $n = 19$ and PS19-T2^{R47H}, $n = 15$). Data are presented as mean ± SEM. Significance was determined using an unpaired, 2-tailed Mann-Whitney test due to the nonparametric data set. $^{**}P < 0.01$, $^{***}P < 0.001$, $^{****}P < 0.0001$. (**G**) Heatmap analysis of microglial gene expression in 9-month-old PS19-T2^{CV} and PS19-T2^{R47H} piriform cortex generated by hierarchical gene clustering based on genotypes. DAM genes, disease-associated microglia genes. For IL-1α, P2ry12, and TNF-α, significance was determined by an unpaired, 2-tailed Student's *t* test. For Apoe, Cst7, IL-1β, and IL-6, significance was determined using an unpaired, 2-tailed Mann-Whitney test due to the nonparametric data set. For all other analyses, significance was determined by an unpaired, 2-tailed *t* test with Welch's correction due to significantly different variances. $^*P < 0.05$, $^{**}P < 0.01$, $^{***}P < 0.001$, $^{****}P < 0.0001$ (PS19-T2^{CV}, $n = 11$ and PS19-T2^{R47H}, $n = 10$).

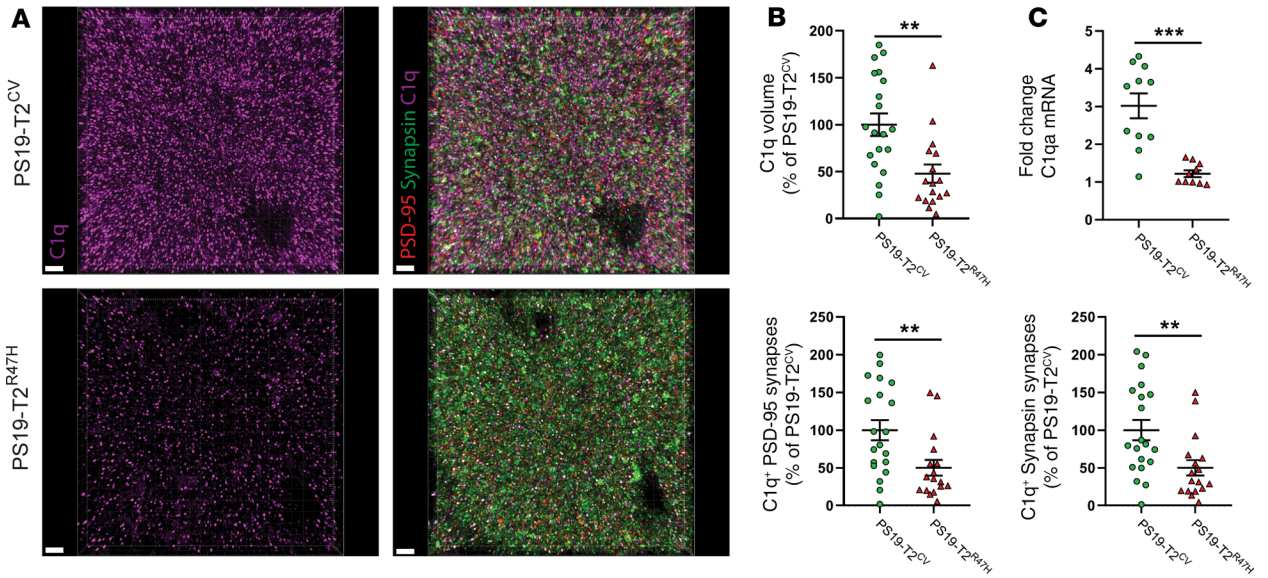

Figure 5. R47H variant of TREM2 lowers C1q⁺ synaptic markers in 9-month-old PS19 mice. (**A**) Representative images from confocal analysis of presynaptic (synapsin in green) and postsynaptic (PSD-95 in red) markers, and C1q (purple) of 9-month-old PS19-T2^{CV} and PS19-T2^{R47H} piriform cortex. Scale bars: 3 μm. Quantification of the percentage of C1q volume (**B**), C1q⁺ PSD-95 puncta number (**D**), and C1q⁺ synapsin puncta number (**E**) (PS19-T2^{CV}, n = 20 and PS19-T2^{R47H}, n = 17). (**C**) Expression of cortical C1qa mRNA in 9-month-old PS19-T2^{CV} and PS19-T2^{R47H} mice (PS19-T2^{CV}, n = 11 and PS19-T2^{R47H}, n = 10). Data are presented as mean ± SEM. Significance was determined using an unpaired, 2-tailed Mann-Whitney test due to the nonparametric data set. $^{**}P < 0.01$, $^{***}P < 0.001$.

likely reason for this effect is that decreased TREM2 function leads to a decreased microglial response to Aβ deposition, increased Aβ-associated local neurotoxicity, and an exacerbation of Aβ-induced tau seeding and spreading (15, 42, 43). However, during the time course of AD, Aβ aggregation and accumulation in the neocortex occurs over a 15- to 25-year period before symptom onset. Tau aggregation and pathology development in the neocortex does not occur until just a few years before the onset of cognitive decline. Thus, while TREM2 signaling may protect against Aβ-related changes in the brain, the role of TREM2 signaling during the neocortical tau phase (symptomatic phase) of AD and in primary tauopathies may not be the same. This is critical to understand, as therapeutic targeting of TREM2 may differ depending on the stage of the disease. Our study unveils a role of TREM2 in the control of tau-mediated synaptic elimination and neurodegeneration in the setting of pure tauopathy that may also be relevant to the neocortical tau phase of AD. Surprisingly, we demonstrated that the AD-associated TREM2^{R47H} variant strongly reduces the development of brain atrophy, as well as synapse loss in PS19 mice. Importantly, in the presence of TREM2^{R47H}, tau phosphorylation was decreased, suggesting that p-tau pathogenesis might be influenced by TREM2 function. Further analysis revealed decreased microglial activation and reduced expression of several DAM genes in PS19-T2^{R47H} mice. These results indicate that TREM2 contributes to the microglial response to tau pathology or tau-mediated impairment. Importantly, a decrease in phagocytosis of postsynaptic elements by microglia expressing TREM2^{R47H} was detected in PS19 mice and AD patients and can, at least in part, explain the decrease in synaptic damage observed in PS19-T2^{R47H} mice. Finally, we observed that microglia expressing TREM2^{R47H} phagocytose fewer synapses due to lower C1q accumulation in synapses, resulting in neuroprotection in the setting of tauopathy.

Although the TREM2^{R47H} variant has been associated with a higher risk of developing AD, we observed delayed progression of p-tau pathology and neurodegeneration in the hippocampus of PS19-T2^{R47H} mice. Surprisingly, in 2 previous studies of PS19 mice with complete absence of TREM2, no change in tau pathology has been reported (25, 26). We do not know the answer to why TREM2^{R47H} decreases some p-tau species at 9 months of age compared with TREM2^{CV} in PS19 mice, whereas TREM2 deletion did not have this effect compared with mice expressing murine TREM2 (25). However, we can speculate that this dissimilarity results from the slightly different age of the mice used between the 2 studies or because of the difference between mouse and human TREM2. Indeed, in the Leyns et al. study (25), the PS19 mice expressed mouse TREM2, which may have a slightly different overall effect compared with human TREM2^{CV} used in this study. Unlike studies on PS19 mice, complete deletion of TREM2 in hTau mice exacerbated tau phosphorylation and insolubility (27). Despite the apparent confusion regarding the impact of TREM2 on tau pathology, we hypothesized that reduced tau pathology in PS19-T2^{R47H} mice results from decreased microglial activation. Indeed, in a mouse model of tau propagation using an injection of the AAV2/6-SYN1 promoter driving the expression of a human P301L tau mutant into the brain, Asai et al. report that depleting microglia dramatically suppressed tau propagation (44). Moreover, microglial activation has been shown to correlate with a deficit in spatial memory and the spread of tau pathology in hTau mice (45). Recently, our lab and others demonstrated that the progression of p-tau pathology is also driven by microglia in PS19 mice (28, 30). Moreover, the same study by Shi et al. (28) demonstrated that microglia-mediated damage was the leading force driving neurodegeneration in a pure-tauopathy mouse model. Similarly, Leyns et al.

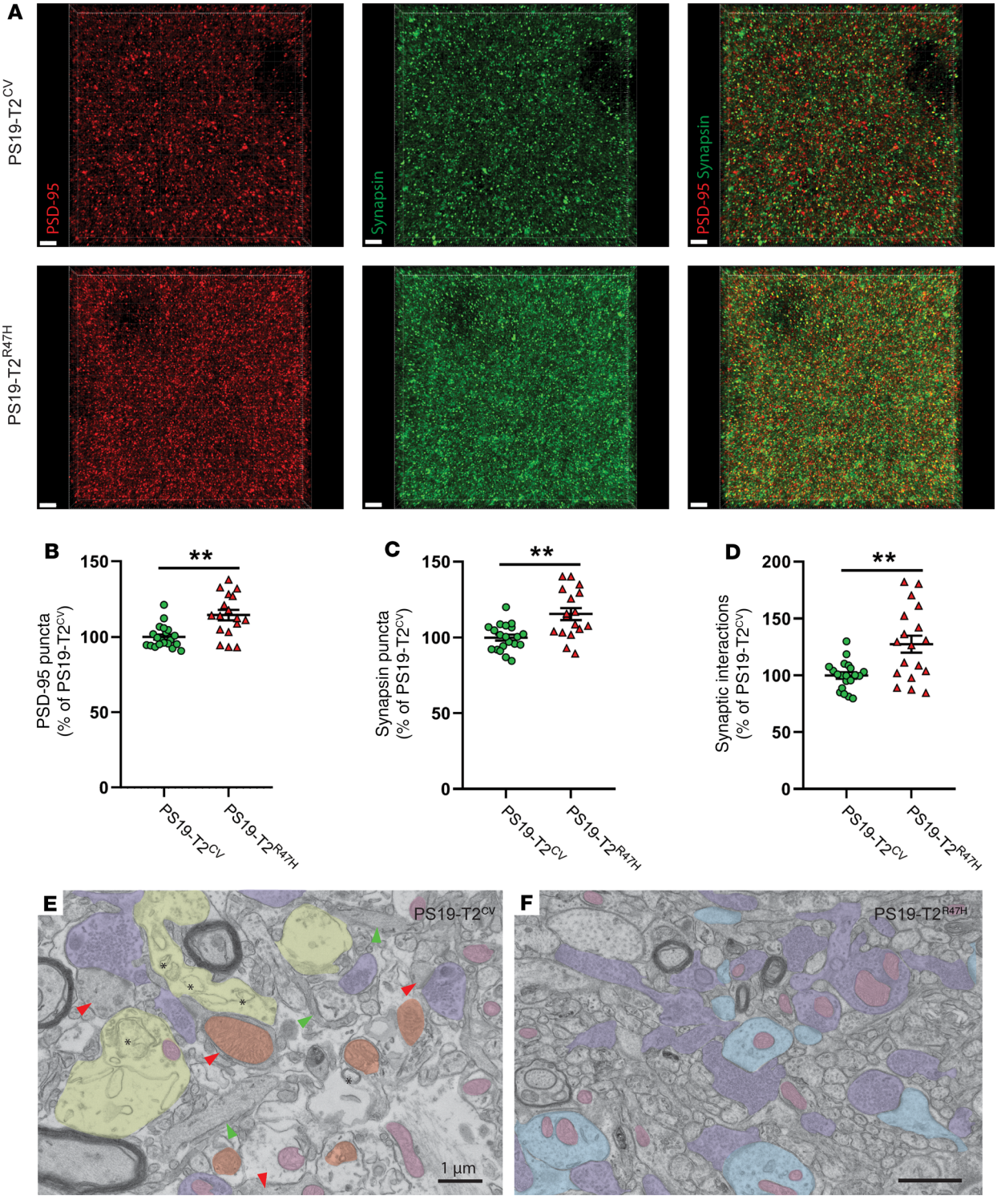

Figure 6. R47H variant of TREM2 reduces synapse loss in 9-month-old PS19 mice. (**A**) Representative images from confocal analysis of presynaptic (synapsin in green) and postsynaptic (PSD-95 in red) markers of 9-month-old PS19-T2^{CV} and PS19-T2^{R47H} piriform cortex. Scale bars: 3 μm. (**B**–**D**) Quantification of puncta numbers from PSD-95 (**B**) and synapsin (**C**) staining, and SEQUIN quantification of synaptic loci (**D**). Data are presented as mean ± SEM. A Mann-Whitney test was used to determine statistical significance for PSD-95 puncta due to the nonparametric data set. For all other graphs, significance was determined by an unpaired, 2-tailed *t* test with Welch's correction due to significantly different variances. $^{**}P < 0.01$ (PS19-T2^{CV}, $n = 20$ and PS19-T2^{R47H}, $n = 17$). (**E** and **F**) Electron microscopic images of the polymorphic layer of the piriform cortex from (**E**) a PS19-T2^{CV} mouse and (**F**) a PS19-T2^{R47H} mouse. Images were obtained at ×9300 and ×6800 magnification, respectively, using an FEI Tecnai Spirit G2 transmission electron microscope. Purple = healthy terminal axons, light blue = healthy dendritic spines, light pink = healthy mitochondria, yellow = dystrophic terminal axons, orange = altered mitochondria, red arrow = dark dendritic spines, green arrow = dark dendrite. Asterisks indicate autophagosomes.

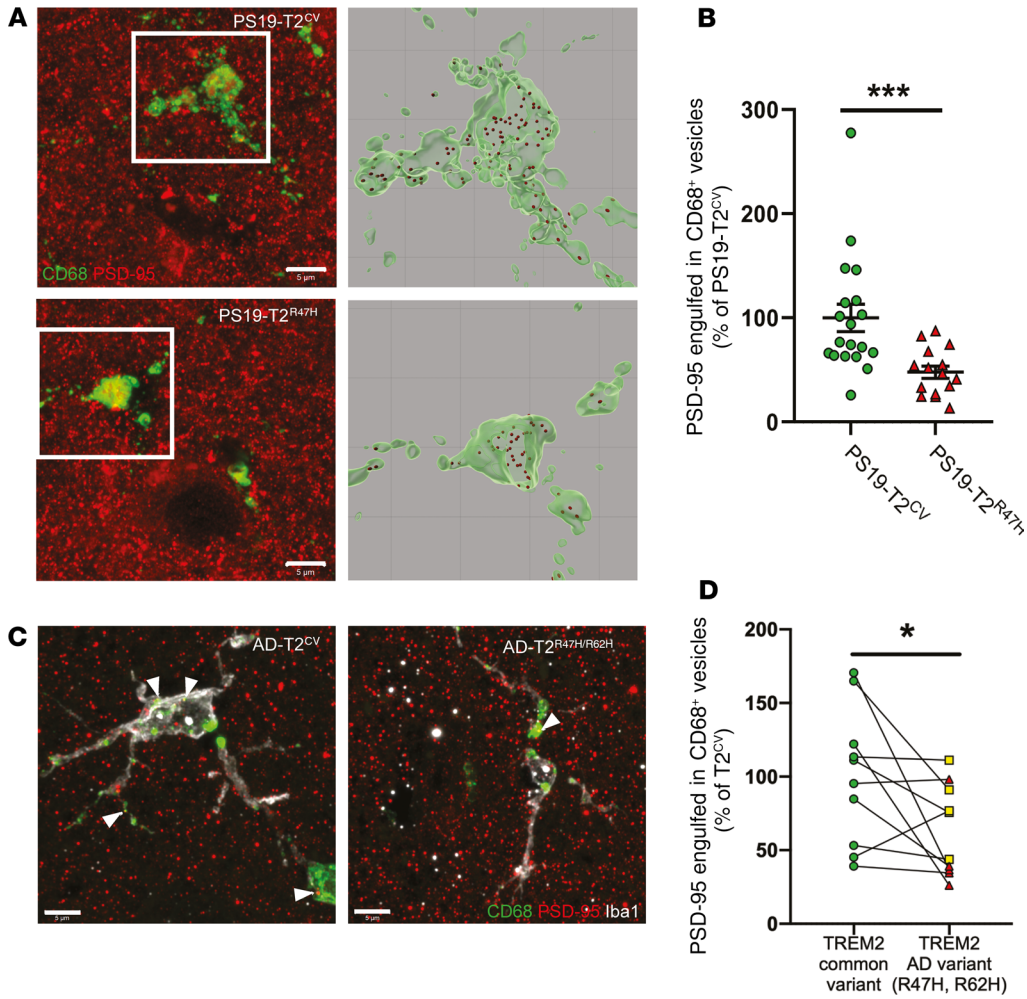

Figure 7. R47H variant of TREM2 alters synapse engulfment by microglia in 9-month-old PS19 mice and human TREM2 variant carriers (R47H and R62H). (**A**) Representative confocal images and relative 3D surface rendering showing volume reconstruction of CD68 (green) and engulfed PSD-95 puncta (red), detected within microglial CD68$^+$ structures of 9-month-old PS19-T2^{CV} and PS19-T2^{R47H} piriform cortex. Scale bars: 5 μm. (**B**) Quantification of engulfed PSD-95 puncta within CD68$^+$ vesicles per microglia. Data are presented as mean ± SEM. Significance was determined using an unpaired, 2-tailed Mann-Whitney test due to the nonparametric data set. ***$P < 0.001$ (PS19-T2^{CV}, $n = 19$ and PS19-T2^{R47H}, $n = 15$). (**C**) Representative image from confocal analysis of microglia (white), CD68 (green), and engulfed PSD-95 puncta (red), detected within microglial CD68$^+$ structures in TREM2^{R47H} (red triangle) and TREM2^{R62H} (yellow square) AD patients (AD-T2$^{R47H/R62H}$) and case-matched TREM2^{CV} AD controls. Scale bars: 5 μm. (**D**) Quantification of engulfed PSD-95 puncta within CD68$^+$ structures (arrowheads) per microglia. Data are presented as mean ± SEM. Significance determined by paired, 2-sided *t* test. *$P < 0.05$ (AD-T2^{CV}, $n = 9$; AD-T2^{R47H}, $n = 5$; and AD-T2^{R62H}, $n = 5$).

and Sayed et al. previously reported that complete loss of TREM2 protects against tau-mediated brain atrophy as well as lower microgliosis (25, 26). Importantly, even though we observed decreased tau pathology in PS19-T2^{R47H} mice, the neuroprotective effect by TREM2^{R47H} characterized in this study is likely attributable to reduced microglia-dependent neuronal damage rather than a direct effect on p-tau pathology per se. Indeed, decreased tau pathology in the piriform cortex has been observed only with p.Thr231, while preserved brain volume, pyramidal layer thickness, and synaptic integrity is reported in the piriform cortex of PS19-T2^{R47H} mice as well as a strong reduction of microgliosis. Moreover, Leyns et al. previously reported a neuroprotection induced by TREM2 deletion in PS19 mice without a change in tau pathology but with lower microgliosis (25). Thus, diminished microgliosis resulting from the R47H variant of TREM2 seems to explain the brain atrophy attenuation in PS19 mice observed in this study. Because synapse loss is well characterized in mouse models of tauopathies (29, 46–48), and TREM2 has been shown to play a key role in synaptic pruning during brain development (39), we then hypothesized that TREM2 loss of function leads to lower brain atrophy in PS19 mice by inhibiting synaptic phagocytosis by microglia. Indeed, our lab previously reported higher levels of PSD-95, a postsynaptic marker, in PS19-TREM2-KO compared with PS19 mice (25). We confirmed that PS19-T2^{R47H} mice have strikingly more pre- and postsynaptic markers, as well as better-maintained pre- and postsynaptic interactions compared with PS19-T2^{CV} mice.

Although the TREM2^{R47H} protective effect against tau-mediated brain atrophy and synapse loss seems clear in this study, the possible mechanisms underlying this phenomenon are multiple. First, chronic immune activation is known to result in high levels

of several proinflammatory cytokines such as TNF-α or IL-1β that can induce synaptic excitotoxicity (49–52), and we show that PS19-T2^{R47H} mice have a robust reduction in the expression of TNF-α and IL-1β, as well as several other proinflammatory cytokines compared with PS19-T2^{CV}. Second, as previously mentioned, TREM2 is well known for its functions in promoting microglial cell survival (53) and in cellular phagocytosis (37, 54, 55). Filipello et al. also determined that TREM2 is essential for microglia-mediated synaptic refinement during the early stages of brain development and that TREM2 deletion resulted in impaired synapse elimination (39). Moreover, a recent study by Sheng at al. reported that TREM2 deficiency ameliorates synaptic deficits in 8-month-old APP/PS1 mice, an amyloid mouse model (56). In PS19-T2^{R47H} mice, we confirmed the reduction of microglial phagocytic properties with fewer CD68^{+} phagolysosomes within microglia. In addition, a decrease in number of postsynaptic puncta engulfed in CD68^{+} vesicles was observed not only in PS19-T2^{R47H} mice, but also in AD patients harboring either the R47H mutation or the R62H mutation, another AD-associated TREM2 variant (41, 57, 58). These data suggest that partial loss of function induced by AD-associated TREM2 variants might protect against aberrant synaptic phagocytosis by microglia due to chronic inflammation. The impaired phagocytosis of synapses by microglia might also be due to lower C1q accumulation in synapses. C1q, the initiating protein of the classical complement cascade, is increased and associated with synapses before overt amyloid plaque deposition in AD and inhibition of C1q reduces the number of phagocytic microglia, as well as the extent of early synaptic loss in familial AD-mutant hAPP (J20) transgenic mice (59). More recently, Dejanovic et al. (34) reported a striking accumulation of complement C1q in synapses of PS19 mice and AD patients. Moreover, they demonstrated an association of synaptic C1q accumulation with augmented microglial engulfment of synapses and a decrease in synapse density in vitro. Interestingly, we reported that despite more synapses in PS19-T2^{R47H} mice, there was dramatically less C1q-opsonized synapsin and fewer PSD-95 puncta detected in the brain of these mice in comparison with PS19-T2^{CV} mice. This is consistent with lower C1q accumulation in synapses of PS19-T2^{R47H} mice compromising the signal for microglia to engulfed them, preserving synaptic density. Importantly, a combination of all these mechanisms resulting from the inhibition of a chronic inflammatory vicious circle remains conceivable here.

Obviously, an evident question emerges from this study: how does TREM2^{R47H} increase the risk of developing AD, but appear protective against tau-mediated synapse loss? The answer might be amyloid, tau, and time dependent. Recently, we have found that TREM2 deficiency increases amyloid-induced tau spreading (42), which is a phase of AD pathogenesis that precedes the tau-linked neurodegeneration phase of AD. In this study (42), we showed that TREM2-KO or the AD-associated TREM2^{R47H} variant reduces microgliosis around Aβ plaques. Importantly, TREM2-KO and the AD-associated TREM2^{R47H} variant strongly promoted tau seeding and spreading in the form of neuritic plaque tau aggregates. In addition, decreased plaque-associated microgliosis in these mice corresponded with higher periplaque Aβ42 accumulation and formation of neuritic dystrophy around plaques. These findings demonstrate a critical role for TREM2 in microglia in inhibiting a key element of Aβ-facilitated tau pathology. Therefore, we hypothesize that AD-associated TREM2 variants increase AD risk by promoting Aβ-mediated local toxicity and facilitate tau seeding and spreading in the early pathological stages of the disease. However, in the later stages of the disease (i.e., symptomatic stage) and in primary tauopathies, when substantial tau pathology has developed, AD-associated TREM2 variants might slow down tau-mediated synapse loss in the brain through reduction of synapse phagocytosis by microglia. It is important to note that complete loss of function of TREM2 in humans results in Nasu-Hakola disease characterized by cerebral degeneration and white matter damage (60, 61). However, partial loss of function of TREM2 as seen with the TREM2^{R47H} mutation in the heterozygous or homozygous condition is associated with increased risk for AD (not with Nasu-Hakola disease) (9, 10, 62). Thus, it may be that decreasing but not ablating TREM2 function during the tau phase of neurodegeneration results in neuroprotection not only in mouse models but also in humans.

Taken together, our data show that TREM2 plays a key role in neurodegeneration in the context of tau pathology. Surprisingly, the AD-associated TREM2^{R47H} variant was strongly neuroprotective, probably because of decreased chronic inflammation and decreased synaptic phagocytosis. While research on microglia and TREM2 in AD has largely focused on TREM2 interactions with Aβ pathology, this study suggests that TREM2 can directly affect tau pathology and tau-mediated neurodegeneration in the brain. This study raises new important questions about targeting TREM2 as a therapeutic approach to treat AD. Indeed, stimulating the TREM2 pathway using antibodies or drugs is thought to be a promising therapeutic strategy to treat or slow down AD progression. However, this study suggests that TREM2 exacerbates tau-mediated neurodegeneration in the later stages of the disease when tau pathology is prominent. This study highlights the complexity of using TREM2 as a target to treat AD or a primary tauopathy. Moving forward, it will be important to identify and establish the appropriate therapeutic window using close monitoring of neurodegenerative stage and inflammation-related AD biomarkers to either stimulate or inhibit the TREM2 pathway based on the disease and its stage. This should be possible with the use of fluid- and imaging-based biomarkers. Importantly, this study revealed for the first time to our knowledge that the AD-associated TREM2^{R47H} variant is protective against tau pathology and tau-mediated neurodegeneration.

Methods

Animals. PS19 transgenic mice expressing human P301S 1N4R mutated tau driven by the PrP promoter were purchased from The Jackson Laboratory (stock 008169). PS19 mice were backcrossed and maintained on a mouse TREM2-KO background (T2KO). PS19-T2KO were crossed with mice that had been engineered using BAC technology to express either human TREM2^{CV} or the AD-associated TREM2^{R47H} on a mouse T2KO background (15). These BAC transgenic mice carrying human TREM2 (common variant or R47H variant), TREML1, and TREML2 were backcrossed with T2KO mice to yield mice that express either TREM2^{CV} or TREM2^{R47H} in the absence of mouse TREM2. The use of BAC TREM2 models prohibited the ability to compare littermates with different genotypes in this study. Because of the fact that male PS19 mice at different ages

have greater tau pathology and neurodegeneration, and less variability than female mice (63, 64), only males were used for analysis in this study. All mice were on the C57BL/6 background.

Sample collection. At time of death, mice were anesthetized with i.p. pentobarbital (200 mg/kg). Blood samples were collected in EDTA-treated tubes before cardiac perfusion with with 3 U/mL heparin in cold Dulbecco's PBS. Blood samples were spun down (10 minutes, 2000 *g*, 4°C), and blood plasma was collected. Brains were carefully extracted and cut into 2 hemispheres. The left hemisphere was collected for immunostaining and fixed in 4% paraformaldehyde overnight before being transferred to 30% sucrose and stored at 4°C until they were sectioned. Brains were cut coronally into 50-μm sections on a freezing sliding microtome (Leica, SM1020R) and stored in cryoprotectant solution (0.2 M PBS, 15% sucrose, 33% ethylene glycol) at –20°C until use. The right hemisphere was dissected to isolate the hippocampus and the cortex for biochemical analysis, and the tissue was kept at –80°C until analyzed.

For electron microscopy, 3 mice per group were anesthetized with i.p. pentobarbital (200 mg/kg) and perfused with 0.1% glutaraldehyde in 4% paraformaldehyde (65). Fifty-micrometer-thick coronal sections of the brain were cut in sodium phosphate buffer using a vibratome (Vibratome series 1000 sectioning system) and stored at –20°C in cryoprotectant until further processing (66).

Volumetric analysis of brains sections. Every sixth brain section (300 μm between sections) starting rostrally at bregma –1.23 mm to the dorsal end of the hippocampus at bregma –2.73 mm were mounted on slides and allowed to dry overnight for each mouse. The following day, mounted sections were stained with 0.1% Sudan black in 70% ethanol at room temperature for 20 minutes, then washed in 70% ethanol 3 times for 1 minute. The sections were washed in Milli-Q water and coverslipped with Fluoromount (Southern Biotech). Slides were imaged with the NanoZoomer 2.0-HT system (Hamamatsu Photonics) and areas of interest measured using the NDP viewer software (Hamamatsu Photonics). The volume for each region of interest was calculated using the following formula: volume = (summary of areas) × 0.3 mm.

Neuronal layer thickness measurement. Three sections (bregma –2.0, –2.4, and –2.8 mm) per mouse were mounted and allowed to dry overnight. The following day, sections were stained in cresyl violet for 6 minutes at room temperature. The slices were then sequentially dehydrated in increasing ethanol concentrations followed by xylene and coverslipped with Cytoseal 60 (Thermo Fisher Scientific, 8310-16). The thickness of the pyramidal cell layer of the piriform cortex and dentate gyrus granular cell layer was measured by drawing a scale perpendicular to the cell layer in all 3 slices and taking the average value for each mouse.

Brain extraction and tau and p-tau ELISA. Half of the hippocampus was weighed and homogenized using a pestle with 20 μL buffer/mg tissue (10 mM Tris-HCl pH 7.4, 0.8 M NaCl, 1 mM EDTA, 2 μM DTT, cOmplete and PhosStop [both Roche], and 10% sucrose). Samples were centrifuged for 10 minutes at 10,000 *g* and 4°C. Supernatant was removed and kept on ice while the pellet was re-homogenized in the same volume of buffer with a sonicator at 30% amplitude, 1 second on/1 second off pulse, for 1 minute, and centrifuged for 10 minutes at 10,000 *g* and 4°C. The 2 supernatants were pooled together and frozen until used. The concentration of tau and p-tau was quantified by sandwich ELISA as previously described (42) using Tau-5 (in-house antibody) as the coating antibody and human-specific biotinylated HT7 for detection for tau ELISA and using HJ14.5 (in-house p.Thr181-tau antibody) as the coating antibody and human-specific biotinylated AT8 for detection for p-tau ELISA. Briefly, 96-well half-area plates were coated with 20 μg/mL of either HJ14.5 or Tau-5 antibody and incubated at 4°C overnight. The next day, the plate was blocked in 3% BSA (RPI Corp.) in PBS for 1 hour at 37°C. Next, peptide standards and samples were diluted in sample buffer (0.25% BSA/PBS, 1× protease inhibitor, 300 mM Tris pH 7.4, PBS), loaded onto the plate, and incubated at 4°C overnight. On the third day, 0.3 μg/mL of biotinylated AT8 for p-tau ELISA (Thermo Fisher Scientific, MN1020B) or biotinylated HT7 for tau ELISA (Thermo Fisher Scientific, MN1000B) was applied to the plate for 1.5 hours at 37°C, and then Streptavidin-poly-HRP-40 (1:10,000 for tau and 1:6,000 for p-tau) (Fitzgerald) was applied for 1.5 hours at room temperature. TMB Superslow Substrate solution (MilliporeSigma) was added and the plates were read at 650 nm on a BioTek plate reader after developing for 30 minutes at room temperature. All samples were run in duplicate.

Immunohistochemistry. For staining microglia (Iba1, rabbit polyclonal, 1:5,000; Wako, 019-19741) and p-tau (AT8, mouse monoclonal, 1:500; Thermo Fisher Scientific, MN1020B — AT180, mouse monoclonal, 1:500; Thermo Fisher Scientific, MN1040 — PG5, mouse monoclonal, 1:500 [gift from Peter Davies, Feinstein Institutes for Medical Research, Northwell Health, Manhasset, New York, USA]), sections were washed 3 times in TBS for 5 minutes and blocked in 0.3% hydrogen peroxide for 10 minutes. After washing, sections were blocked in 3% milk in TBS with 0.25% Triton X-100 (TBSX) for 30 minutes. Primary antibody was diluted in 3% milk/TBSX, and the sections were incubated in the primary antibody overnight at 4°C. The next day, sections were washed and incubated with secondary antibody diluted in 3% milk/TBSX for 1 hour. For AT8 staining, after washing, sections were incubated in ABC Elite solution (VectaStain, PK-6100) for 1 hour, prepared following the manufacturer's instructions, followed by another washing step. For Iba1, AT180, and PG5 staining, after washing, sections were incubated with HRP-conjugated secondary antibodies for 1 hour at room temperature (1:500; Jackson Laboratory, 111-035-003). Sections were developed in DAB solution (Vector Laboratories, SK4103), washed, and mounted on slides. After drying overnight, the slides were dehydrated in increasing ethanol concentrations followed by xylene and coverslipped with Cytoseal 60 (Thermo Fisher Scientific, 8310). Slides were scanned on the NanoZoomer 2.0-HT system. Images were further processed and quantified with the use of Fiji software version 1.51. All areas were quantified in 2 to 3 sections (300 μm apart from each other) per mouse.

Immunofluorescence. Immunofluorescence staining was performed as previously described (36). Briefly, free-floating tissue was placed in 12-well plates with Netwell inserts (Corning) containing PBS. Blocking solution and primary and secondary antibody mixtures were centrifuged at 17,000 *g* for 5 minutes just before use. Tissue was rinsed 3 times, 5 minutes each, in PBS followed by blocking in 20% normal goat serum (NGS) in PBS for 1 hour at room temperature. Tissue was then incubated overnight at room temperature with primary antibodies (CD68, rat monoclonal, 1:500; AbD SeroTec, MCA1957), Iba1 (goat polyclonal, 1:5,000; Abcam, ab5076), PSD-95 (rabbit polyclonal, 1:200; Thermo Fisher Scientific, 51-6900), synapsin-1/2 (guinea pig polyclonal, 1:500; Synaptic Systems, 106004),

and C1q (mouse monoclonal, 1:50; Abcam, ab71940) in 10% NGS containing 0.3% Triton X-100 in PBS. The following day, sections were rinsed 3 times, 5 minutes each, in PBS followed by incubation in secondary antibodies (Thermo Fisher Scientific; 1;500) in 10% NGS containing 0.3% Triton X-100 in PBS for 4 hours at room temperature. Sections were mounted, dried at room temperature, briefly rinsed in distilled water, and then coverslipped. Mounting medium (~150 μL/slide) was prepared the day of use by mixing Tris-MWL 4-88 (Electron Microscopy Sciences, 17977-150) with AF300 (Electron Microscopy Sciences, 17977-25) at a 9:1 ratio.

Image acquisition for immunofluorescence. Images were acquired on an LSM 880 microscope with AiryScan detector (Zeiss). Quantification was performed using a semiautomated pipeline based on MATLAB (MathWorks) and Imaris 9.3.1 software (Bitplane) as previously described (36). Spots were detected for each channel using an *x-y* size of 0.2 μm, a *z* size of 0.6 μm, and automated background subtraction. A 0.1-μm *x-y* and 0.3-μm *z* guard was applied to exclude spots intersecting the edge of the image volume. Synaptic loci were identified using custom MATLAB scripts from Sauerbeck (36) to find the nearest neighbor based on the *x-y-z* centroid of the top 20% brightest puncta. A cutoff of 270 nm pre-to-postsynaptic separation was used to quantify synaptic loci for Figure 6 from the frequency distribution of pre-to-postsynaptic separations. Complement labeling of synaptic loci was performed with Imaris 9.3.1 software by creating a surface of C1q staining based on a threshold applied to all images and by counting the number of pre- and postsynaptic spots positive for this surface. Three images per mouse were obtained in the polymorphic layer of the piriform cortex for this analysis.

Quantification of confocal images for Iba1 and CD68 was performed on a semiautomated platform using MATLAB and Imaris 9.3.1 software to create surfaces of each stain based on a threshold applied to all images and colocalize Iba1 and CD68 surfaces to evaluate the volume of $CD68^+$ vesicles within $Iba1^+$ cells. For quantification of the number of PSD-95 puncta engulfed in $CD68^+$ phagolysosomes, the PSD-95 puncta previously detected were automatically counted within the $CD68^+$ surface per microglia using Imaris 9.3.1 software. Three to 5 microglia were imaged for each mouse or subject.

Immunofluorescence of human tissue. Paraffin-embedded 8-μm sections were dewaxed in xylene for 6 minutes twice, followed by rehydration descending ethanol to water (100% [twice], 95%, 90%, 70%, 30%, and 10% ethanol, followed by 100% water [twice]). For antigen retrieval, slides were incubated for 45 minutes in citrate buffer, pH 6. Slides were incubated in 0.1% Sudan black solution in 70% ethanol for 20 minutes to eliminate autofluorescence. After PBS washes, sections were blocked in 10% normal donkey serum and 0.3% Triton X-100 for 1 hour and then placed in primary antibodies overnight at 4°C in blocking solution: CD68 (mouse monoclonal, 1:100; DAKO, M0876), Iba1 (goat polyclonal, 1:500; Abcam, ab5076), and PSD-95 (rabbit polyclonal, 1:200, Thermo Fisher Scientific, 51-6900). The following day, sections were washed, placed in secondary antibodies for 2 hours (Thermo Fisher Scientific; 1:500), and then washed again 3 times for 20 minutes each and mounted. Mounting medium was prepared the day of use by mixing Tris-MWL 4-88 (Electron Microscopy Sciences, 17977- 150) with AF300 (Electron Microscopy Sciences, 17977-25) at a 9:1 ratio followed by vortexing and bench-top centrifugation to remove bubbles. High-precision 1.5H coverglasses were used for all experiments. Human samples were obtained from the Alzheimer's Disease Research Center at Washington University. $TREM2^{R47H}$ and $TREM2^{R62H}$ AD cases were paired with $TREM2^{CV}$ AD cases matching age, sex, and *APOE* genotype (Supplemental Table 1).

Gene expression. We extracted total RNA from mouse cortex with the RNeasy Mini Kit (QIAGEN) and prepared cDNA with the High-Capacity RNA-to-cDNA kit (Applied Biosystems), following manufacturers' instructions. Gene expression analysis was performed using microarray in collaboration with the Genome Technology Access Core at Washington University. Using TaqMan probes, the relative gene expression was quantitatively measured using Fluidigm Biomark HD with integrated fluidic circuits.

Tissue preparation for electron microscopy. Three PS19-$T2^{CV}$ mice and 2 PS19-$T2^{R47H}$ mice were used for electron microscopy. In each animal, brain sections containing the polymorphic layer of the piriform cortex (bregma –1.67 mm to –1.91mm) were selected based on the stereotaxic atlas of Paxinos and Franklin (67). The sections were washed 3 times, 10 minutes each, with PBS, pH 7.4, and then incubated 1 hour in a solution of equal volume of 3% potassium ferrocyanide in phosphate buffer (PB, 0.1 M, pH 7.4) and 4% aqueous osmium tetroxide. Following washing 3 times, 5 minutes each in PBS, tissues were incubated 20 minutes in a thiocarbohydrazide solution and washed again 3 times, 5 minutes each in double-distilled water (ddH_2O). A 30-minute incubation of 2% osmium tetroxide (from 4% stock, diluted in ddH_2O) was then performed. The brain sections were washed 3 times, 5 minutes each in ddH_2O and dehydrated with an increasing amount of ethanol (5-minute washes each): 35% (twice), 50%, 70%, 80%, 90%, 100% (thrice). After dehydration in ethanol, the sections were washed 3 times, 5 minutes each, in propylene oxide and were emerged overnight in Durcupan resin. The following day, tissues were placed between 2 ACLAR sheets (Electron Microscopy Sciences) covered with a thin layer of resin and incubated 3 days at 55°C to polymerize.

Ultramicrotomy and transmission electron microscopy. The polymorphic layer of the piriform cortex was excised from the ACLAR sheet with a razor blade and glued onto a resin block. The tissues were then cut using an ultramicrotome (Leica Ultracut UC7), first with a thickness of 300 nm to confirm the region of interest using toluidine blue, and finally at a thickness of 70 nm. The ultrathin sections were collected onto copper-mesh grids. The polymorphic layer was imaged at 80 kV using a transmission electron microscope (FEI Tecnai Spirit G2) equipped with a Hamamatsu ORCA-HR digital camera (10 MP). The user was blinded to the experimental conditions during imaging and ultrastructural interpretation. Images of the synaptic neuropil were randomly acquired throughout the region of interest so as to avoid bias. Sixteen to 20 nonoverlapping images at a magnification between ×6,800 and ×13,500 were obtained per animal. Overall, between 575 μm^2 and 729 μm^2 of the synaptic neuropil were imaged per animal.

Images were analyzed using the software ImageJ (NIH). For the qualitative analysis of synaptic ultrastructure, the following parameters were considered: the presence and size of autophagosomes; the presence of altered mitochondria; the presence of dark dendrites, dendritic spines, or axon terminals; and the presence of dystrophic synapses. Dark cells (e.g., microglia, neurons) are characterized by ultrastructural signs of oxidative stress (endoplasmic reticulum dilation, condensation of the nucleoplasm and cytoplasm, altered mitochondria) (68,

69) and have been seen previously in pathological conditions, such as AD (70). Axon terminals were recognized by their inclusion of multiple synaptic vesicles. Dendritic spines were recognized and differentiated from dendrites by their size and presence of a postsynaptic density (71). Dark synaptic elements were recognized by their electron-dense cytoplasm (72). Altered mitochondria were distinguished from normal ones by their large increase in size and/or a disruption of their cristae and/or outer membrane structure (73). Dystrophic synapses were defined by the presence of autophagosomes, a reduced number of synaptic vesicles, and a swollen shape (seen as an increase in size and/or electron-lucent content). Autophagosomes were recognized by their circular shape and delineating double membrane (74).

Statistics. Unless otherwise stated, all data are presented as mean ± SEM. GraphPad Prism 8.0.0 was used to perform statistical analyses. Gaussian distribution was evaluated using the D'Agostino-Pearson normality test. Statistical analysis was performed using 2-tailed Student's unpaired *t* test under normal distribution. In case of unequal variances, Welch's correction was used with the Student's unpaired *t* test. If samples deviated from normal distribution, statistical analysis was performed using a Mann-Whitney test. For human data, significance was determined by paired 2-tailed *t* test. *P* less than 0.05 was considered significant: $^{*}P < 0.05$, $^{**}P < 0.01$, $^{***}P < 0.001$, and $^{****}P < 0.0001$ versus PS19-T2^{CV}.

Study approval. All animal experimental protocols were approved by the Animal Studies Committee at Washington University, St. Louis, Missouri, USA.

Author contributions

MG, MC, JDU, and DMH designed the study. MG, CEGL, ADS, MKSP, MX, NK, JRS, TTK, and MET performed the experiments and analyzed the data. MG, JDU, and DMH wrote the manuscript. All authors discussed the results and commented on the manuscript.

Acknowledgments

This study was supported by the McDonnell Center for Cellular and Molecular Neurobiology (to MG), NIH grant AG047644, the JPB Foundation, the Charles and Helen Schwab Foundation (to DMH), and the Edward N. and Della L. Thome Memorial Foundation, Bank of America, N.A., Trustee (to DMH). Scanning of immunohistochemistry was performed on the NanoZoomer digital pathology system courtesy of the Hope Center Alafi Neuroimaging Laboratory. Confocal data were generated on a Zeiss LSM 880 Airyscan Confocal Microscope, which was purchased with support from the Office of Research Infrastructure Programs (ORIP), a part of the NIH Office of the Director under grant OD021629, and in part with support from the Washington University Center for Cellular Imaging (WUCCI) supported by Washington University School of Medicine, The Children's Discovery Institute of Washington University and St. Louis Children's Hospital (CDI-CORE-2015-505 and CDI-CORE-2019-813), and the Foundation for Barnes-Jewish Hospital (3770 and 4642). We thank the Genome Technology Access Center in the Department of Genetics at Washington University School of Medicine for help with genomic analysis. The Center is partially supported by NCI Cancer Center Support grant P30 CA91842 to the Siteman Cancer Center and by ICTS/CTSA grant UL1 TR000448 from the National Center for Research Resources (NCRR), a component of the NIH, and NIH Roadmap for Medical Research. This publication is solely the responsibility of the authors and does not necessarily represent the official view of the NCRR or the NIH. The authors specifically thank David Blum for his helpful advice during the study.

Address correspondence to: David M. Holtzman, Washington University School of Medicine, 660 South Euclid Avenue, Box 8111, St. Louis, Missouri 63110, USA. Phone: 314.747.0644; Email: holtzman@wustl.edu.

1. Alzheimer's Association. Alzheimer's disease facts and figures. *Alzheimers Dement*. 2016;12(4):459–509.
2. Holtzman DM, Morris JC, Goate AM. Alzheimer's disease: the challenge of the second century. *Sci Transl Med*. 2011;3(77):77sr1.
3. Castellani RJ, Rolston RK, Smith MA. Alzheimer disease. *Dis Mon*. 2010;56(9):484–546.
4. Serrano-Pozo A, Frosch MP, Masliah E, Hyman BT. Neuropathological alterations in Alzheimer disease. *Cold Spring Harb Perspect Med*. 2011;1(1):a006189.
5. Leyns CEG, Holtzman DM. Glial contributions to neurodegeneration in tauopathies. *Mol Neurodegener*. 2017;12(1):50.
6. Keren-Shaul H, et al. A unique microglia type associated with restricting development of Alzheimer's disease. *Cell*. 2017;169(7):1276–1290.e17.
7. Krasemann S, et al. The TREM2-APOE pathway drives the transcriptional phenotype of dysfunctional microglia in neurodegenerative diseases. *Immunity*. 2017;47(3):566–581.e9.
8. Zhang ZG, Li Y, Ng CT, Song YQ. Inflammation in Alzheimer's disease and molecular genetics: recent update. *Arch Immunol Ther Exp (Warsz)*. 2015;63(5):333–344.
9. Guerreiro R, et al. TREM2 variants in Alzheimer's disease. *N Engl J Med*. 2013;368(2):117–127.
10. Jonsson T, et al. Variant of TREM2 associated with the risk of Alzheimer's disease. *N Engl J Med*. 2013;368(2):107–116.
11. Schmid CD, et al. Heterogeneous expression of the triggering receptor expressed on myeloid cells-2 on adult murine microglia. *J Neurochem*. 2002;83(6):1309–1320.
12. Bouchon A, Hernández-Munain C, Cella M, Colonna M. A DAP12-mediated pathway regulates expression of CC chemokine receptor 7 and maturation of human dendritic cells. *J Exp Med*. 2001;194(8):1111–1122.
13. Gratuze M, Leyns CEG, Holtzman DM. New insights into the role of TREM2 in Alzheimer's disease. *Mol Neurodegener*. 2018;13(1):66.
14. Wang Y, et al. TREM2 lipid sensing sustains the microglial response in an Alzheimer's disease model. *Cell*. 2015;160(6):1061–1071.
15. Song WM, Joshita S, Zhou Y, Ulland TK, Gilfillan S, Colonna M. Humanized TREM2 mice reveal microglia-intrinsic and -extrinsic effects of R47H polymorphism. *J Exp Med*. 2018;215(3):745–760.
16. Ulrich JD, et al. Altered microglial response to Aβ plaques in APPPS1-21 mice heterozygous for TREM2. *Mol Neurodegener*. 2014;9:20.
17. Jay TR, et al. TREM2 deficiency eliminates TREM2^{+} inflammatory macrophages and ameliorates pathology in Alzheimer's disease mouse models. *J Exp Med*. 2015;212(3):287–295.
18. Cheng-Hathaway PJ, et al. The Trem2 R47H variant confers loss-of-function-like phenotypes in Alzheimer's disease. *Mol Neurodegener*. 2018;13(1):29.
19. Long JM, Holtzman DM. Alzheimer disease: an update on pathobiology and treatment strategies. *Cell*. 2019;179(2):312–339.
20. Piccio L, et al. Cerebrospinal fluid soluble TREM2 is higher in Alzheimer disease and associated with mutation status. *Acta Neuropathol*. 2016;131(6):925–933.
21. Suárez-Calvet M, et al. sTREM2 cerebrospinal fluid levels are a potential biomarker for microglia activity in early-stage Alzheimer's disease and associate with neuronal injury markers. *EMBO Mol Med*. 2016;8(5):466–476.
22. Lill CM, et al. The role of TREM2 R47H as a risk factor for Alzheimer's disease, frontotemporal lobar degeneration, amyotrophic lateral sclerosis, and Parkinson's disease. *Alzheimers Dement*. 2015;11(12):1407–1416.
23. Cruchaga C, et al. GWAS of cerebrospinal fluid tau levels identifies risk variants for Alzheimer's disease. *Neuron*. 2013;78(2):256–268.
24. Buerger K, et al. CSF phosphorylated tau protein correlates with neocortical neurofibrillary pathology in Alzheimer's disease. *Brain*.

2006;129(pt 11):3035–3041.
25. Leyns CEG, et al. TREM2 deficiency attenuates neuroinflammation and protects against neurodegeneration in a mouse model of tauopathy. *Proc Natl Acad Sci U S A*. 2017;114(43):11524–11529.
26. Sayed FA, et al. Differential effects of partial and complete loss of TREM2 on microglial injury response and tauopathy. *Proc Natl Acad Sci U S A*. 2018;115(40):10172–10177.
27. Bemiller SM, et al. TREM2 deficiency exacerbates tau pathology through dysregulated kinase signaling in a mouse model of tauopathy. *Mol Neurodegener*. 2017;12(1):74.
28. Shi Y, et al. Microglia drive APOE-dependent neurodegeneration in a tauopathy mouse model. *J Exp Med*. 2019;216(11):2546–2561.
29. Yoshiyama Y, et al. Synapse loss and microglial activation precede tangles in a P301S tauopathy mouse model. *Neuron*. 2007;53(3):337–351.
30. Mancuso R, et al. CSF1R inhibitor JNJ-40346527 attenuates microglial proliferation and neurodegeneration in P301S mice. *Brain*. 2019;142(10):3243–3264.
31. Deming Y, et al. The *MS4A* gene cluster is a key modulator of soluble TREM2 and Alzheimer's disease risk. *Sci Transl Med*. 2019;11(505):eaau2291.
32. Liddelow SA, et al. Neurotoxic reactive astrocytes are induced by activated microglia. *Nature*. 2017;541(7638):481–487.
33. Shi Y, et al. ApoE4 markedly exacerbates tau-mediated neurodegeneration in a mouse model of tauopathy. *Nature*. 2017;549(7673):523–527.
34. Dejanovic B, et al. Changes in the synaptic proteome in tauopathy and rescue of tau-induced synapse loss by C1q antibodies. *Neuron*. 2018;100(6):1322–1336.e7.
35. Collman F, Buchanan J, Phend KD, Micheva KD, Weinberg RJ, Smith SJ. Mapping synapses by conjugate light-electron array tomography. *J Neurosci*. 2015;35(14):5792–5807.
36. Sauerbeck AD, et al. SEQUIN multiscale imaging of mammalian central synapses reveals loss of synaptic connectivity resulting from diffuse traumatic brain injury. *Neuron*. 2020;107(2):257–273.e5.
37. Takahashi K, Rochford CD, Neumann H. Clearance of apoptotic neurons without inflammation by microglial triggering receptor expressed on myeloid cells-2. *J Exp Med*. 2005;201(4):647–657.
38. Hsieh CL, et al. A role for TREM2 ligands in the phagocytosis of apoptotic neuronal cells by microglia. *J Neurochem*. 2009;109(4):1144–1156.
39. Filipello F, et al. The microglial innate immune receptor TREM2 is required for synapse elimination and normal brain connectivity. *Immunity*. 2018;48(5):979–991.e8.
40. Jin SC, et al. Coding variants in TREM2 increase risk for Alzheimer's disease. *Hum Mol Genet*. 2014;23(21):5838–5846.
41. Sims R, et al. Rare coding variants in PLCG2, ABI3, and TREM2 implicate microglial-mediated innate immunity in Alzheimer's disease. *Nat Genet*. 2017;49(9):1373–1384.
42. Leyns CEG, et al. TREM2 function impedes tau seeding in neuritic plaques. *Nat Neurosci*. 2019;22(8):1217–1222.
43. Zhou Y, et al. Human and mouse single-nucleus transcriptomics reveal TREM2-dependent and TREM2-independent cellular responses in Alzheimer's disease. *Nat Med*. 2020;26(1):131–142.
44. Asai H, et al. Depletion of microglia and inhibition of exosome synthesis halt tau propagation. *Nat Neurosci*. 2015;18(11):1584–1593.
45. Maphis N, et al. Reactive microglia drive tau pathology and contribute to the spreading of pathological tau in the brain. *Brain*. 2015;138(pt 6):1738–1755.
46. van Olst L, et al. Microglial activation arises after aggregation of phosphorylated-tau in a neuron-specific P301S tauopathy mouse model. *Neurobiol Aging*. 2020;89:89–98.
47. Hoffmann NA, Dorostkar MM, Blumenstock S, Goedert M, Herms J. Impaired plasticity of cortical dendritic spines in P301S tau transgenic mice. *Acta Neuropathol Commun*. 2013;1:82.
48. Kopeikina KJ, et al. Synaptic alterations in the rTg4510 mouse model of tauopathy. *J Comp Neurol*. 2013;521(6):1334–1353.
49. Zhao J, O'Connor T, Vassar R. The contribution of activated astrocytes to Aβ production: implications for Alzheimer's disease pathogenesis. *J Neuroinflammation*. 2011;8:150.
50. Becker D, Zahn N, Deller T, Vlachos A. Tumor necrosis factor alpha maintains denervation-induced homeostatic synaptic plasticity of mouse dentate granule cells. *Front Cell Neurosci*. 2013;7:257.
51. Tachida Y, et al. Interleukin-1 beta up-regulates TACE to enhance alpha-cleavage of APP in neurons: resulting decrease in Abeta production. *J Neurochem*. 2008;104(5):1387–1393.
52. Kitazawa M, et al. Blocking IL-1 signaling rescues cognition, attenuates tau pathology, and restores neuronal β-catenin pathway function in an Alzheimer's disease model. *J Immunol*. 2011;187(12):6539–6549.
53. Zheng H, et al. TREM2 promotes microglial survival by activating Wnt/β-catenin pathway. *J Neurosci*. 2017;37(7):1772–1784.
54. Kawabori M, et al. Triggering receptor expressed on myeloid cells 2 (TREM2) deficiency attenuates phagocytic activities of microglia and exacerbates ischemic damage in experimental stroke. *J Neurosci*. 2015;35(8):3384–3396.
55. Atagi Y, et al. Apolipoprotein E is a ligand for triggering receptor expressed on myeloid cells 2 (TREM2). *J Biol Chem*. 2015;290(43):26043–26050.
56. Sheng L, et al. Microglial Trem2 induces synaptic impairment at early stage and prevents amyloidosis at late stage in APP/PS1 mice. *FASEB J*. 2019;33(9):10425–10442.
57. Song W, et al. Alzheimer's disease-associated TREM2 variants exhibit either decreased or increased ligand-dependent activation. *Alzheimers Dement*. 2017;13(4):381–387.
58. Jin SC, et al. Coding variants in TREM2 increase risk for Alzheimer's disease. *Hum Mol Genet*. 2014;23(21):5838–5846.
59. Hong S, et al. Complement and microglia mediate early synapse loss in Alzheimer mouse models. *Science*. 2016;352(6286):712–716.
60. Paloneva J, et al. Mutations in two genes encoding different subunits of a receptor signaling complex result in an identical disease phenotype. *Am J Hum Genet*. 2002;71(3):656–662.
61. Bianchin MM, et al. Nasu-Hakola disease (polycystic lipomembranous osteodysplasia with sclerosing leukoencephalopathy--PLOSL): a dementia associated with bone cystic lesions. From clinical to genetic and molecular aspects. *Cell Mol Neurobiol*. 2004;24(1):1–24.
62. Slattery CF, et al. R47H TREM2 variant increases risk of typical early-onset Alzheimer's disease but not of prion or frontotemporal dementia. *Alzheimers Dement*. 2014;10(6):602–608.e4.
63. Zhang B, et al. The microtubule-stabilizing agent, epothilone D, reduces axonal dysfunction, neurotoxicity, cognitive deficits, and Alzheimer-like pathology in an interventional study with aged tau transgenic mice. *J Neurosci*. 2012;32(11):3601–3611.
64. Yanamandra K, et al. Anti-tau antibodies that block tau aggregate seeding in vitro markedly decrease pathology and improve cognition in vivo. *Neuron*. 2013;80(2):402–414.
65. Ligorio M, Descarries L, Warren RA. Cholinergic innervation and thalamic input in rat nucleus accumbens. *J Chem Neuroanat*. 2009;37(1):33–45.
66. Tremblay ME, Riad M, Majewska A. Preparation of mouse brain tissue for immunoelectron microscopy. *J Vis Exp*. 2010;(41):2021.
67. Paxinos G, Franklin KBJ. *Paxinos and Franklin's the Mouse Brain in Stereotaxic Coordinates*. 4th ed. Academic Press; 2012.
68. Bisht K, et al. Dark microglia: A new phenotype predominantly associated with pathological states. *Glia*. 2016;64(5):826–839.
69. Tremblay MÈ, Zettel ML, Ison JR, Allen PD, Majewska AK. Effects of aging and sensory loss on glial cells in mouse visual and auditory cortices. *Glia*. 2012;60(4):541–558.
70. El Hajj H, et al. Ultrastructural evidence of microglial heterogeneity in Alzheimer's disease amyloid pathology. *J Neuroinflammation*. 2019;16(1):87.
71. Peters A, Palay SL, Webster HdeF. *The fine structure of the nervous system: The neurons and supporting cells*. 3rd ed. Oxford University Press; 1991.
72. Johnson JE. The occurrence of dark neurons in the normal and deafferentated lateral vestibular nucleus in the rat: observations by light and electron microscopy. *Acta Neuropathol*. 1975;31(2):117–127.
73. St-Pierre MK, Bordeleau M, Tremblay MÈ. Visualizing dark microglia. *Methods Mol Biol*. 2019;2034:97–110.
74. Smith PY, et al. miR-132/212 deficiency impairs tau metabolism and promotes pathological aggregation in vivo. *Hum Mol Genet*. 2015;24(23):6721–6735.